Dynamics of Interactions Involving Deformable Drops: Hydrodynamic Dimpling under Attractive and Repulsive Electrical Double Layer Interactions

Rogério Manica,[†] Jason N. Connor,[‡,§] Steven L. Carnie,*[,†] Roger G. Horn,[‡] and Derek Y. C. Chan[†]

Particulate Fluids Processing Centre, Department of Mathematics and Statistics, The University of Melbourne, Parkville, Victoria 3010, Australia, Ian Wark Research Institute, University of South Australia, Mawson Lakes, SA 5095, Australia, and PELM Centre, Central Queensland University, Gladstone, Queensland 4680, Australia

Received July 18, 2006. In Final Form: October 5, 2006

A model developed previously to analyze force measurements between two deformable droplets in the atomic force microscope [*Langmuir* **2005**, *21*, 2912−2922] is used to model the drainage of an aqueous film between a mica plate and a deformable mercury drop for both repulsive and attractive electrical double-layer interactions between the mica and the mercury. The predictions of the model are compared with previously published data [*Faraday Discuss.* **2003**, *123*, 193−206] on the evolution of the aqueous film whose thickness has been measured with subnanometer precision. Excellent agreement is found between theoretical results and experimental data. This supports the assumptions made in the model which include no-slip boundary conditions at both interfaces. Furthermore, the successful fit attests to the utility of the model as a tool to explore details of the drainage mechanisms of nanometer-thick films in which fluid flow, surface deformations, and colloidal forces are all involved. One interesting result is that the model can predict the time at which the aqueous film collapses when attractive mica−mercury forces are present without the need to invoke capillary waves or other local instabilities of the mercury/electrolyte interface.

1. Introduction

Central to understanding the dynamics of interactions in soft matter, for example, suspensions of emulsion drops or cellular components of biological systems, is the interplay between colloidal forces such as van der Waals, electrical double-layer and steric forces, hydrodynamic interactions arising from relative motion within the suspension medium, surface tension forces, and internal Laplace pressure effects. These interactions give rise to surface deformations, which in turn determine the relative importance and contributions of various forces.

Recently, advances have been made in using the atomic force microscope (AFM) to measure the force between two oil drops (stabilized by surfactants) that have been driven together or pulled apart under well-controlled conditions.[1,2] For drops of around 50 μm radius, the range of velocities studied cover the range of thermal velocities for drops in this size range. The strong dependence of the total interaction force on the relative velocity of approach and retraction demonstrated the importance of hydrodynamic effects. The variations of such measured forces with relative velocity, surface tension, and surface charge of the drops are well accounted for by a quantitative model that includes the explicit roles of hydrodynamic interactions, drainage of the thin aqueous film between the interacting drop, surface forces, and interfacial deformations.[3] The good agreement between experiment and theory, which only requires independently determined system parameters, provided confidence in using the theoretical model to give further details about the deforming surface such as surface velocity at different parts of the interface and the flow pattern and shear rates of the draining aqueous film during interaction. However, current experiments based on the AFM are as yet unable to provide direct information about the deformations of the interfaces during the course of interaction.

On the other hand, a complementary experimental technique based on using the surface force apparatus (SFA) as an imaging device is well-suited to yield accurate details of the evolution of the surface profiles of drop deformation during interaction. Through analysis by video recording of fringes of equal chromatic order (FECO), Connor and Horn[4] were able to measure the space−time evolution of the deformations of a mercury/aqueous electrolyte interface due to hydrodynamic and electrical double-layer interactions with an approaching mica plate. The position of the deformable interface was determined with subnanometer precision for a mercury drop of radius ∼2 mm and mica velocity in the range 20−70 μm/s. As the surface potential of the mercury drop could be controlled independently, it was possible to study surface deformations under a range of repulsive and attractive interactions due to electrical double-layer interactions between the mercury and the mica interface. In particular, the SFA measurements are able to track deformations of the interface from a near-parabolic shape at large separations from the mica, to the formation and development of the characteristic dimple[5−7] as the separation decreases, and finally to the resolution of the dimple to a flat, stable film, in the case of repulsive interaction between the mica and the mercury or to the collapse of an unstable aqueous film when the mica−mercury interaction is attractive.

* stevenlc@unimelb.edu.au.
[†] The University of Melbourne.
[‡] University of Southern Australia.
[§] Central Queensland University.

(1) Dagastine, R. R.; Stevens, G. W.; Chan, D. Y. C.; Grieser, F. *J. Colloid Interface Sci.* **2004**, *273*, 339.
(2) Dagastine, R. R.; Manica, R.; Carnie, S. L.; Chan. D. Y. C.; Stevens, G. W.; Grieser, F. *Science* **2006**, *313*, 210.
(3) Carnie, S. L.; Chan, D. Y. C.; Lewis, C.; Manica, R.; Dagastine, R. R. *Langmuir* **2005**, *21*, 2912.
(4) Connor, J. N.; Horn, R. G. *Faraday Discuss.* **2003**, *123*, 193.
(5) Frankel, S. P.; Mysels, K. J. *J. Phys. Chem.* **1962**, *66*, 190.
(6) Hartland, S.; Robinson, J. D. *J. Colloid Interface Sci.* **1977**, *60*, 72.
(7) Dimitrov, D. S.; Ivanov, I. B. *J. Colloid Interface Sci.* **1978**, *64*, 97.

10.1021/la0620760 CCC: $37.00
Published on Web 12/06/2006

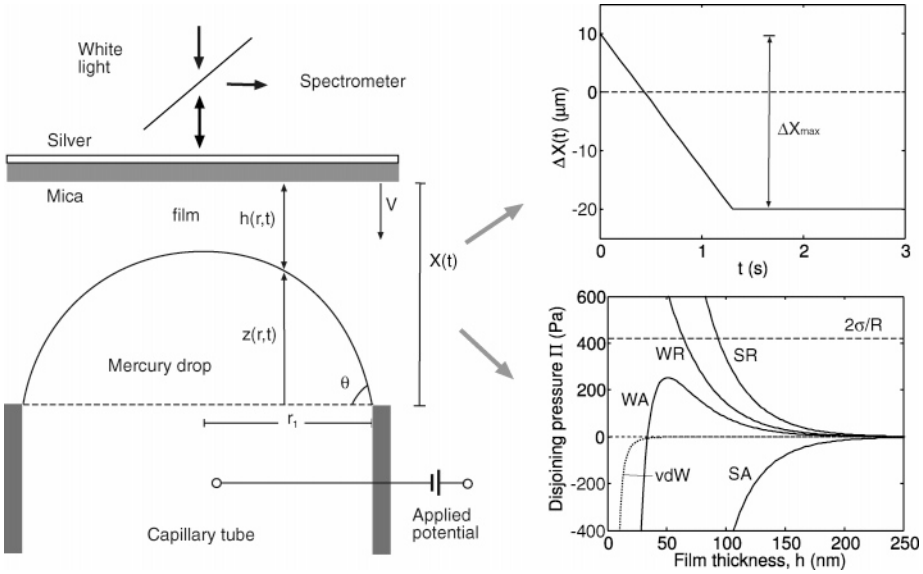

Figure 1. Schematic diagram of a mica surface approaching a mercury drop. Top inset: Variation of the position of the mica with time. Bottom inset: Disjoining pressures due to electrical double-layer interaction designated as strongly repulsive (SR), weakly repulsive (WR), weakly attractive (WA), and strongly attractive (SA) as calculated from the nonlinear Poisson−Boltzmann theory. The disjoining pressure due to van der Waals (vdW) forces is shown as the dotted line, and the magnitude of the Laplace pressure ($2\sigma/R$) is indicated by the horizontal dashed line.

The aim of this paper is to undertake a detailed comparison between results of the Connor−Horn experiments on deformations of the mercury/electrolyte interface with the theoretical model developed to model force data between deformable drops acquired on the AFM. A new boundary condition at the edge of the thinning film has been developed to model actual experimental conditions and to enforce conservation of volume of the deforming drop. This comparison with experiments will explore the range of applicability of the theory to macroscopic drop sizes and also test its applicability under conditions of both attractive and repulsive surface forces. The results also provide insight into the hydrodynamic boundary condition for the drainage of nanometer-thick aqueous electrolyte films confined between the mica and a deformable mercury/electrolyte interface. Other details such as flow patterns, interfacial velocities, and shear rates in draining films under repulsive and attractive electrical double-layer forces can also be inferred from the theory.

The structure of the paper is as follows. In section 2, we summarize the main features of the SFA experimental setup and define key system parameters. The governing equations and assumptions of the model are discussed in section 3. Detailed comparisons between theory and experiment under repulsive and attractive surface forces are given in section 4. In section 5, we present theoretical results relating to details of fluid flow in the draining film and deformations of the mercury interface. The paper closes with a discussion.

2. The SFA Experiment

A schematic representation of the Connor−Horn SFA experimental system is shown in Figure 1. White light optical interference between reflections from the silver and mercury surfaces is analyzed with the aid of a spectrometer, which allows the silver−mercury distance and hence the aqueous film thickness h to be determined over a range of r, where r is the horizontal distance from the symmetry axis passing through the top of the drop. Readers should consult the original paper[4] for full details. A mercury drop is formed at the top of a sealed capillary of radius 1.5 mm immersed in an aqueous electrolyte solution of 0.1 mM KCl. At this electrolyte concentration, the mica has a surface potential of −100 mV. The potential difference between the mercury and a reference calomel electrode in the bulk electrolyte can be adjusted by an external potential source. As a result, the equilibrium electrical double-layer interaction between the mica and the mercury surfaces can be made to be repulsive or attractive.

Detailed experimental studies have been undertaken for four cases of such interactions, designated strongly repulsive (SR), weakly repulsive (WR), weakly attractive (WA), and strongly attractive (SA). The force per unit area or the disjoining pressure, $\Pi(h)$, of these four cases as functions of the separation, h, between a flat mica and flat mercury surface are shown in the inset of Figure 1. The nonlinear Poisson−Boltzmann theory is used to calculate these results. In comparison to the electrical double-layer interactions, the magnitude of the attractive van der Waals interaction is negligibly small at the range of film thicknesses of interest (>50 nm). For this system, the nonlinear Poisson−Boltzmann theory is able to account accurately for measurements of equilibrium film thickness.[8]

The capillary radius r_1 is 1.5 mm, but with slight flattening of the mercury drop due to gravity, the radius of curvature, R, of the mercury at the apex is measured to be 1.9 mm. The interfacial tension, σ, of the mercury−electrolyte interface is 426 mN/m when the applied potential is near its point of zero charge (the WR and WA cases) and slightly lower, 420 mN/m, when the applied potential has a magnitude of $\pm\sim$450 mV for the SR and SA cases. The viscosity μ of the electrolyte is taken to be 0.89 mPa s at a temperature of 25 °C. Mercury has a viscosity of 1.53 mPa s.

In the experimental protocol, the (rigid) mica plate is driven toward the fixed mercury drop at a constant velocity, V (nominally 23 μm/s but as high as 67 μm/s in one case), for a total travel distance ΔX_{max} that ranges from 15 to 30 μm from an initial distance of closest approach h_0 that varies between 5 and 20 μm. Thus, the mica plate is driven toward the mercury surface for around 1 s and is then held at the final position. In response, the mercury/electrolyte interface is observed to deform in an axially

(8) Connor, J. N.; Horn, R. G. *Langmuir* **2001**, *17*, 7194.

symmetric manner, and the separation between the mercury surface and the mica surface, $h(r, t)$ can be deduced from variations of the shape of the FECO with position and time. The separation $h(r, t)$ can be determined with subnanometer resolution in the direction normal to the mica surface and micrometer resolution in the r direction.

At large mica−mercury separations, the mercury/electrolyte interface has a near-parabolic shape with the point of closest approach at the axis of symmetry ($r = 0$). As the separation decreases, the interface will develop a characteristic dimple shape where the minimum separation between the mica and the mercury will no longer be at the axis of symmetry. Instead, the minimum separation will occur at a radial distance r_{rim} (>0) at what is sometimes called the barrier rim. If the disjoining pressure is sufficiently repulsive, the mercury interface will eventually be flattened by its interaction with the mica surface and separated from it by an equilibrium aqueous film of thickness h_{eq}.[8] If the disjoining pressure is sufficiently attractive at small separations, the aqueous film will drain away completely, and the mercury surface will collapse onto the mica surface. In approaching either final state, hydrodynamic pressures in the film cause the mercury/electrolyte interface to exhibit the familiar dimpling at intermediate separations.

3. Governing Equations

We model the mercury−mica system by adapting recent work of Carnie et al.[3] which analyzed AFM measurements of the force between two oil drops in relative motion in an electrolyte solution. Even though those drops had radii of around 40 μm and the mercury drop in the present SFA experiment has radius around 2 mm, both systems are described by essentially the same equations. The reason is that both systems contain large differences in scale between the drop radius, the radial extent of deformations, and the minimum film thickness—for the SFA experiments, these are ∼2 mm, ∼100 μm, and ∼100 nm, respectively, which then justifies the use of simplified hydrodynamics, as the aqueous film between the mica and the mercury forms on approach and subsequently drains.

The large difference in length scales implies the weak variation of the film thickness with a typical radial scale and implies

$$\frac{\partial h}{\partial r} \ll 1 \tag{1}$$

which satisfies the requirements of lubrication theory[9] and the study of thin films generally.[10] The validity of this condition has been discussed extensively in the works of Chesters.[11−13]

The hydrodynamic flow under the usual thin-film assumptions is a pressure-driven axisymmetric radial flow. The form of the flow depends on the hydrodynamic boundary conditions assumed at the liquid/liquid and solid/liquid interfaces. Our previous work dealt with oil droplets coated with anionic surfactant which is known to "immobilize" the surface and leads to a no-slip boundary condition at the oil/water interface.[2] In the present case, however, the validity of a no-slip boundary condition at the mercury/electrolyte interface is far less evident, since mercury is only about 50% more viscous than water, and special care has been taken to ensure that the experiments were carried out under clean conditions. Nevertheless, as an initial attempt, we shall analyze our results using the no-slip boundary condition both at the mica/electrolyte interface and an assumed no-slip boundary condition at the mercury/electrolyte interface. This means we do not need to determine the flow inside the mercury, which greatly simplifies the model. We note that other workers also observed that experimental results for film drainage agree with no-slip boundary conditions rather than the full-slip condition that assumes the continuity of tangential stress across the liquid/liquid interface.[14] However, after a comparison with experiments under the no-slip condition, we will return to consider the possible effects of including hydrodynamic slip in the boundary conditions.

With the above assumptions, the radial flow has a parabolic profile in the normal direction, which leads to the familiar film-thinning equation[20]

$$\frac{\partial h}{\partial t} = \frac{1}{12\mu r}\frac{\partial}{\partial r}\left(rh^3\frac{\partial p}{\partial r}\right) \tag{2}$$

where $h(r, t)$ is the film thickness as a function of radial coordinate r and time t, $p(r, t)$ is the excess hydrodynamic pressure in the film relative to the bulk liquid, and μ is the assumed Newtonian film viscosity.

Surface tension forces are introduced through a normal force balance at the mercury/electrolyte interface with interfacial tension σ

$$p + \Pi = \frac{2\sigma}{R} - \frac{\sigma}{r}\frac{\partial}{\partial r}\left(r\frac{\partial h}{\partial r}\right) \tag{3}$$

where R is the radius at the apex of the drop, and $\Pi(h)$ is the disjoining pressure. Equation 3 is obtained by using the thin film approximation[10] to simplify the expression of the mean curvature of the interface. The use of a pressure between flat surfaces to describe surface forces is due to Derjaguin.[15] Because the film thickness is so weakly varying in the radial scale, we can use the disjoining pressure at the local separation $h(r)$ with negligible error. Unlike our earlier work[3] which only had repulsive double-layer forces acting at large separations, here we need to describe both repulsive and attractive double-layer forces and at smaller separations relative to the Debye length. For these reasons, we use a numerical solution of the nonlinear Poisson−Boltzmann equation[16] using the algorithm of Chan et al.[17,18]

Early works modeling film drainage start from these assumptions.[5−7] Numerical treatment of these equations dates from the work of Hartland[19] and refined by Slattery,[20] who described the drainage once a dimple had been formed. Surface forces were incorporated via a disjoining pressure in ref 21. A detailed asymptotic study of the formation and subsequent drainage of a dimple was given by Yiantsios and Davis[22,23] for interaction under constant force such as that due to buoyancy effects. They also described the conditions on the drop/continuum-phase viscosity ratio under which the interface can be regarded as immobile. If these conditions are not met, one expects "partial

(9) Reynolds, O. *Philos. Trans. R. Soc. London, Ser. A* **1886**, *A177*, 157.
(10) Leal, G. *Laminar flow and convective transport processes*; Butterworth Heinemann: Burlington, MA, 1992.
(11) Abid, S.; Chesters, A. K. *Int. J. Multiphase Flow* **1994**, *20*, 613.
(12) Saboni, A.; Gourdon, C.; Chesters, A. K. *J. Colloid Interface Sci.* **1995**, *175*, 27.
(13) Bazhlekov, I. B.; Chesters, A. K.; van de Vosse, F. N. *Int. J. Multiphase Flow* **2000**, *26*, 445.
(14) Klaseboer, E.; Chevaillier, J. Ph.; Gourdon, C.; Masbernat, O. *J. Colloid Interface Sci.* **2000**, *229*, 274.
(15) Derjaguin, B. V. *Kolloid-Z.* **1934**, *69*, 155.
(16) Hunter, R. J. *Foundations of Colloid Science*, 2nd ed.; Clarendon Press: Gloucestershire, 2001.
(17) Chan, D. Y. C.; Pashley, R. M.; White, L. R. *J. Colloid Interface Sci.* **1980**, *77*, 283.
(18) MacCormack, D.; Carnie, S. L.; Chan, D. Y. C. *J. Colloid Interface Sci.* **1995**, *169*, 177.
(19) Hartland, S. *Chem. Eng. Prog. Symp. Ser.* **1969**, *65*, 82.
(20) Lin, C.-Y.; Slattery, J. C. *AIChEJ* **1982**, *28*, 147.
(21) Chen, J.-D *J. Colloid Interface Sci.* **1984**, *98*, 329.
(22) Yiantsios, S. G.; Davis, R. H. *J. Fluid Mech.* **1990**, *217*, 547.
(23) Yiantsios, S. G.; Davis, R. H. *J. Colloid Interface Sci.* **1991**, *144*, 412.

mobility" at the fluid/fluid interface, and fluid circulation inside the drop needs to be taken into account.

Chesters has made detailed numerical studies of drops with either mobile or partially mobile interfaces at constant force[12] or at constant velocity.[11,13] The constant velocity case was characterized by the boundary condition

$$\frac{\partial h}{\partial t} = -V \tag{4}$$

applied at some large radial distance r_{max}.

In modeling the AFM measurements, where a drop placed on a piezoelectric stage is driven with velocity V toward another drop, eq 4 is not the correct description of the experimental situation. Although the stage is driven at constant velocity V, the separation does not reduce at the same rate due to deformation of the drop once there is a significant force acting on it. Using matched asymptotic expansions, we derived a new boundary condition[3]

$$\frac{\mathrm{d}h}{\mathrm{d}t} + \alpha \frac{\mathrm{d}G}{\mathrm{d}t} = -V \quad \text{at } r = r_{max} \tag{5}$$

which accounts for weak deformations of the drop, where V is the velocity of the piezoelectric stage. In the context of the present SFA experiment, V is the velocity of the mica, and the constant α is given by

$$\alpha = 1 + \frac{1}{2}\ln\left(\frac{{r_{max}}^2}{4R^2}\right) + \frac{1}{2}\ln\left(\frac{1+\cos\theta}{1-\cos\theta}\right) \tag{6}$$

where θ is the angle the drop makes with the capillary at $r = r_1$. The quantity G is related to the force F between the drop and the mica by

$$G = \frac{F}{2\pi\sigma} = \frac{1}{\sigma}\int_0^\infty r[p(r,t) + \Pi(h(r,t))]\,\mathrm{d}r \tag{7}$$

In practice, to be consistent with eq 5, the upper limit of this integral is set to r_{max} in computing G. Provided that r_{max} is sufficiently large (in practice, $r_{max} \approx 350\ \mu$m), the numerical results are independent of r_{max} in the new boundary condition given by eqs 5 and 6. This therefore conforms to the normal expectation that numerical results are independent of the size of the computational domain, provided that the domain is sufficiently large.

Equations 2 and 3 are to be solved numerically over the interval $0 \le r \le r_{max}$, subject to suitable initial conditions and boundary conditions where r_{max} is the largest radial distance at which we compute the profile numerically. The initial condition must be consistent with eq 3 in that it must produce a zero film pressure. This requirement is satisfied by a parabolic surface for the drop as the initial condition

$$h(r, t_{start}) = h_0 + \frac{r^2}{2R} \tag{8}$$

where h_0 is the initial minimum separation $h(0, t_{start})$. Other boundary conditions are

$$\frac{\partial h}{\partial r} = 0 \quad \text{at } r = 0 \tag{9}$$

$$\frac{\partial p}{\partial r} = 0 \quad \text{at } r = 0 \tag{10}$$

$$p = 0 \quad \text{at } r = r_{max} \tag{11}$$

which reflect axisymmetry around $r = 0$ and zero film pressure far from the interaction zone.

On using the Method of Lines with central differences for eqs 2 and 3 and Simpson's rule for eq 7, we obtain a system of differential-algebraic equations of index 1. This set of equations can be solved with a standard numerical package, in our case, ode15s in *Matlab*.[3]

The boundary conditions in eqs 5 and 6 are obtained by matching the inner numerical solution for $r < r_{max}$ to the full outer solution that describes the shape of the entire mercury drop that protrudes from a capillary of radius r_1 in the absence of gravity. In the presence of gravity, the quasi-equilibrium shape of the drop is governed by the Young−Laplace equation

$$\sigma \frac{\mathrm{d}}{\mathrm{d}r}\left[\frac{rz'}{(1+z'^2)^{1/2}}\right] - r\Pi[h(r,t)] - rp(r,t) - r\Delta\rho g z = -\Lambda r \tag{12}$$

where Λ is the Lagrange multiplier associated with enforcing the constant volume constraint, and $\Delta\rho$ is the density difference between the drop and the electrolyte. By introducing the dimensionless variables s, χ

$$r = r_1 s \quad z = r_1 \chi \tag{13}$$

eq 12 in the absence of disjoining pressure Π, and the hydrodynamic pressure, p, can be written as

$$\frac{\mathrm{d}}{\mathrm{d}s}\left[\frac{s\chi'}{(1+\chi'^2)^{1/2}}\right] - \left(\frac{r_1}{\lambda}\right)^2 s\chi = -\frac{\Lambda r_1}{\sigma}\, s \tag{14}$$

This result shows that the effect of gravity is measured by the dimensionless Bond number $Bo = (r_1/\lambda)^2$ where the capillary length λ is given by

$$\lambda = \left(\frac{\sigma}{\Delta\rho g}\right)^{1/2} \tag{15}$$

The Bond number in the present mercury experiment ($Bo \approx 0.6$) is larger than that encountered in the oil drop experiments,[3] both because the drops are larger and because mercury is much denser than water, so the effect of gravity on the static drop shape is not small.

However, if we consider the change in the static profile of the drop under the imposition of a force F at the apex, we can associate with the force a length scale $G = F/(2\pi\sigma)$, and the radial scale of deformations is given by $r_c = \sqrt{r_1 G}$ (see, e.g., refs 24 and 25). The Bond number at the scale of r_c instead of r_1 is $(r_c/\lambda)^2 \approx 0.01 \ll 1$. Typically, we choose our computational domain $r_{max} \approx 2-3r_c$, which means that gravity can be neglected in computing the profile (numerically) in the inner region $r < r_{max}$. Since eq 3 is only used in this inner region, the appropriate value of R is the radius of curvature at the apex, which has been measured experimentally to be 1.9 mm when the mica surface is far from the mercury/electrolyte interface.

Now, the solution of the Young−Laplace equation for a drop in the presence of gravity with an apex radius of curvature $R =$ 1.9 mm and a capillary radius $r_1 = 1.5$ mm produces a nonspherical drop with volume 3.2 mm^3 and a contact angle $\theta = 59.6°$ at the capillary edge $r = r_1$. So, if we wish to treat the drop as a gravity-free spherical drop with radius R being the actual radius of

(24) Chan, D. Y. C.; Dagastine, R. R.; White, L. R. *J. Colloid Interface Sci.* **2001**, *236*, 141.
(25) Bardos, D. C. *Surf. Sci.* **2002**, *517*, 157.

Table 1. Experimental and Theoretical Parameters of the Mercury−Mica System in the Surface Force Apparatus

physical parameter	experiment	theory
	Surface Force Parameters	
mica surface potential	−100 ± 10 mV	−100 mV
drop surface potential	−492 ± 20 mV (SR)	−492 mV
	−12 ± 20 mV (WA)	−24 mV
	408 ± 20 mV (SA)	408 mV
electrolyte concentration, n	0.1 ± 0.01mM KCl	0.11 mM KCl
	Fluid Properties	
viscosity (water), μ	0.89 mPa s	0.89 mPa s
drop surface tension, σ	426 mN/m (SR, SA)	426 mN/m
	420 mN/m (WA)	420 mN/m
drop radius, R, at apex	1.9 ± 0.02 mm	1.9 mm
drop contact angle, θ	52° ± 1°	52°
	SFA Parameters	
maximum mica travel, ΔX_{max}	30 ± 3 μm	24−29 μm
drive velocity, V	23 or 67 ± 2 μm/s	24 or 67 μm/s
initial separation, h_0	10 ± 0.1 μm	10 μm

curvature at the apex of the drop, then the two plausible options are to use either a spherical drop with the same capillary radius r_1 of 1.5 mm but a smaller volume or one with the same volume as the actual drop but with a larger capillary radius. The first choice gives a drop of volume 2.8 mm^3 and a contact angle $\theta = 52.1°$ at $r = r_1$, and this is the value we will use throughout. The second choice requires a capillary radius r_1 of 1.54 mm and a contact angle $\theta = 54.2°$ at the capillary. It turns out that none of the results we present below are sensitive to such small differences in the values of θ.[26]

4. Comparisons Between Experiments and Theory

Theoretical results are computed using the model outlined in the previous section. Input parameters are taken from independent measurements or literature values, and these are summarized in Table 1 together with values used to give theoretical results using our model. The surface potentials for three different cases—SR, WA, and SA—are obtained by subtracting a constant from the applied potential, which was shown in ref 8 to account correctly for the equilibrium drop profile according to the nonlinear Poisson−Boltzmann model.

It was reported in ref 4 that mica was driven toward mercury at a constant speed of 23 μm/s for a set time. In fact, the actual velocity drive function of the mica has a small rise and decay time with a linear acceleration and deceleration ramp. According to the manufacturer of the Nanomover microstepping motors used for the mica drive (Melles Griot, U.S.A.), the acceleration and deceleration rates are 458 μm/s^2. These transients in the velocity function are included as input to our computation, although the effect is only significant when the nominal velocity is high (around 67 μm/s). However, it is found that the drive stop times t_{stop} (when the mica velocity reaches zero) required to fit the data—or equivalently, the maximum mica travel—differ from those quoted in ref 4 in which the deceleration ramp was neglected (see Table 1).

4.1. Strongly Repulsive (SR) Disjoining Pressure. In Figure 2a, we compare experimental measurements and theoretical predictions of the mica−mercury separation $h(r, t)$ for the case in which the interaction is a monotonic strong repulsion—the strongly repulsive (SR) case (see Figure 1). The experimental results are cross sections of an almost perfectly axisymmetric deformation profile. In the experiment, the mica surface, initially

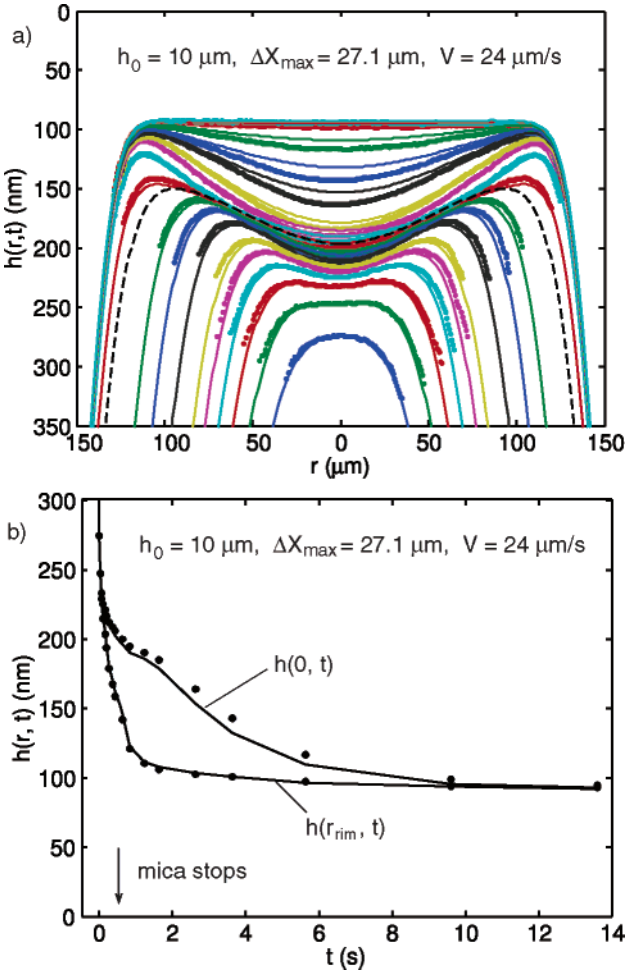

Figure 2. Comparison between theory (lines) and experiment (dots) for the strongly repulsive (SR) case. (a) Drop profiles $h(r, t)$ − from bottom to top: $t = -0.02$, 0.02, 0.06, 0.10, 0.14, 0.18, 0.26, 0.34, 0.42, 0.555 (dashed curve, without data points − mica stops), 0.62, 0.82, 1.22, 1.62, 2.62, 3.62, 5.62, 9.62, and 13.62 s. Note that $t = 0$ corresponds to the time at which the curvature of the profile at $r = 0$ changes sign. (b) Film thickness at the center $h(0, t)$ and at the barrier rim $h(r_{rim}, t)$. The initial separation h_0, mica travel ΔX_{max}, and mica velocity V are indicated in the figure. Again, the dots denote experimental results.

at a separation of $h_0 = 10$ μm from the mercury/electrolyte interface, is driven toward the mercury interface at a nominal constant velocity $V = 23$ μm/s for a total displacement $\Delta X_{max} = 30$ μm. The theoretical curves are calculated using $V = 24$ μm/s for a total displacement $\Delta X_{max} = 27.1$ μm; these values are within experimental error of the nominal values.

The mica−mercury separation $h(r, t)$ during later stages of the approach is shown in Figure 2a when the aqueous film thins down from a thickness of about 300 nm to the final equilibrium thickness of about 100 nm. The time value associated with each $h(r, t)$ profile is relative to the reference time $t = 0$, at which the curvature of the mercury/electrolyte interface at $r = 0$ is observed to change sign and signals the formation of a dimple. There is an uncertainty of one video half-frame or ±0.02 s in determining the value of this reference time.

Our calculations show that, at $t = 0$ where $h(0, t) \approx 300$ nm, the mica surface has already travelled 14 μm, so with an initial separation of $h_0 = 10$ μm, the apex of the mercury drop has already deformed by 4 μm by this time. From $t = 0$ onward, we see that the curvature of the mercury/electrolyte interface changes sign and begins to develop the familiar dimple shape with the associated development of a barrier rim at position $r = r_{rim}$.

(26) Carnie, S. L.; Chan, D. Y. C.; Manica, R. *ANZIAM J.* **2005**, *46* (E), C805.

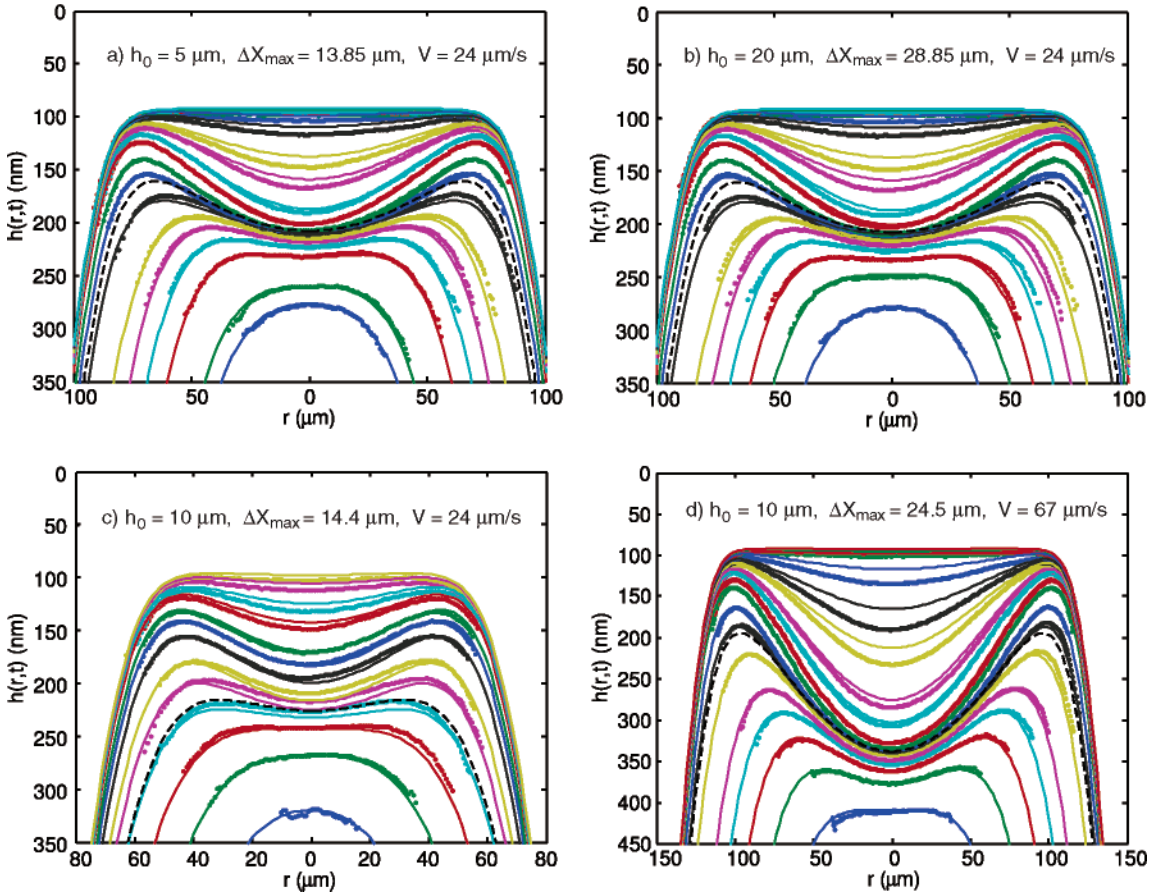

Figure 3. Comparison between theory (lines) and experiment (points) of the mercury/electrolyte interfacial profile $h(r, t)$ for the strongly repulsive (SR) case at various combinations of initial separations h_0, total mica travel ΔX_{max}, and mica velocity V. The dashed curves are theoretical profiles at the instant that the mica drive stops in the computation, and they have no corresponding data points. From bottom to top: (a) $t = -0.02$, 0.0, 0.06, 0.10, 0.14, 0.18, 0.26, 0.313 (dashed curve − mica stops), 0.34, 0.42, 0.62, 0.82, 1.22, 1.62, 2.62, 3.62, 5.62, 9.62, and 13.62 s. (b) $t = -0.02$, 0.0, 0.06, 0.10, 0.14, 0.18, 0.26, 0.313 (dashed curve − mica stops), 0.34, 0.42, 0.62, 0.82, 1.22, 1.62, 2.62, 3.62, 5.62, 9.62, and 13.62 s. (c) $t = -0.04$, 0, 0.04, 0.08, 0.088 (dashed curve − mica stops), 0.12, 0.16, 0.24, 0.32, 0.4, 0.6, 0.8, 1.2, and 1.6 s. (d) $t = 0$, 0.04, 0.08, 0.12, 0.16, 0.24, 0.293 (dashed curve − mica stops), 0.32, 0.4, 0.6, 0.8, 1.2, 1.6, 2.6, 3.6, 5.6, 9.6, and 13.6 s.

Although the mica drive stopped after $t_{stop} = 0.555$ s, where the corresponding profile $h(r, t_{stop})$ is given by the dashed line in Figure 2a, the dimple continues to develop as the deformation relaxes to its equilibrium shape. The thinning profile maintains a high degree of axial symmetry, which justifies our use of an axisymmetric theory to describe the problem.

A comparison of the variation with time of the observed and predicted film thicknesses at the center of the dimple $h(0, t)$ and at the barrier rim $h(r_{rim}, t)$ is given in Figure 2b. Note that the thickness at the barrier rim $h(r_{rim}, t)$ decreases more rapidly with time than the film thickness $h(0, t)$ at the center of the dimple. The interface then takes a further 10 s to attain equilibrium after the mica has stopped moving at $t = 0.555$ s.

At large times, the dimple resolves to an equilibrium flat film with thickness h_{eq} equal to the separation at which the disjoining pressure due to electrical double-layer repulsion is equal to the Laplace pressure of the mercury drop: $\Pi(h_{eq}) = 2\sigma/R$.

In Figure 3, we show similar profiles of the mercury/electrolyte interface for the SR case but with different initial mica−mercury separations, different total displacements of the mica, and different mica velocities. In all cases, the agreement between experiment and theory is very good, with the possible exception of the portion of $h(r, t)$ near $r \approx 0$, for times after the development of the dimple where theory predicts that the film thins too rapidly. Note that the allowance of a partial-slip hydrodynamic boundary condition at the mica/electrolyte or mercury/electrolyte interface would only increase the divergence between experiment and theory. We will suggest a plausible explanation for this discrepancy in the discussion section. In any event, the volume of electrolyte enclosed within the barrier rim differs by less than 4% between the experimental and theoretical profile shapes.

In Figure 4, we show the variation of the position of the barrier rim r_{rim} with time for the SR case for three different total displacements of the mica surface. In all cases, the agreement between experiment and theory is very good. At small times, r_{rim} increases as $t^{1/2}$ as observed in the constant velocity case.[14]

The calculated total pressure profiles that comprise the hydrodynamic pressure p and the disjoining pressure Π profiles within the film at various stages of thinning are shown in Figure 5. Results for the decomposition of the total pressure into the hydrodynamic and electrostatic disjoining pressure components are shown in separate panels. As already noted from analysis of the experimental data,[27] we observe that, while the relative contributions to the total pressure from hydrodynamic effects and from electrostatic effects vary significantly during the thinning process, the total pressure, being the sum of these two contributions, remains remarkably constant across the extent of the film throughout the film thinning process. This can perhaps be expected, because variations of the film thickness, which are on the order of 100 nm, are small compared to the deformation

(27) Horn, R. G.; Asadullah, M.; Connor, J. N. *Langmuir* **2006**, *22*, 2610.

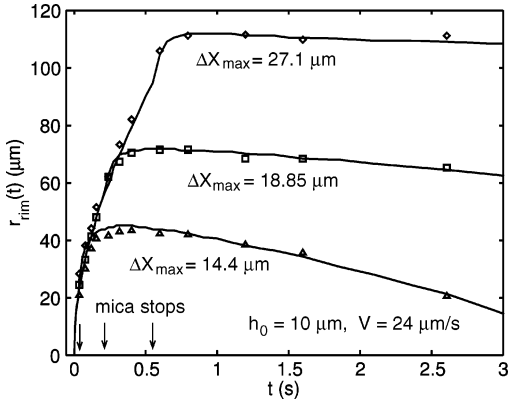

Figure 4. Variations of the barrier rim position $r_{rim}(t)$ with time: experimental results (symbols) and theory (lines) from an initial mica−mercury separation $h_0 = 10\ \mu$m, and a mica velocity $V = 24\ \mu$m/s. The distance travelled by the mica is indicated in the figure and corresponds (from top to bottom) to results shown in Figure 2a, 3b, and 3c, respectively. Arrows indicate the stopping times.

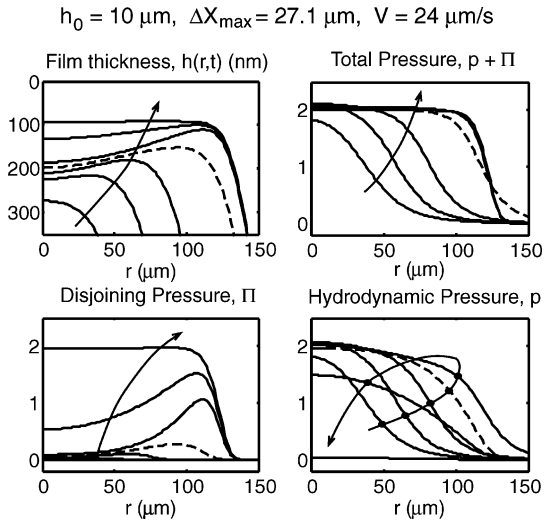

Figure 5. Variations of the hydrodynamic pressure p, disjoining pressure Π, and total pressure $(p + \Pi)$ for the strongly repulsive (SR) case with initial separation $h_0 = 10\ \mu$m, mica travel $\Delta X_{max} = 27.1\ \mu$m, and mica velocity $V = 24\ \mu$m/s (same parameters as results in Figure 2): $t = -0.02$, 0.1, 0.26, 0.555, 1.22, 3.62, and 13.62 s. The arrow indicates increasing time. The dashed curve corresponds to the time when the mica stopped.

zone, which is ~200 μm in radial extent. The radial deformation zone is in turn only a small fraction of the mercury drop, which has dimensions on the millimeter scale (see section 5).

4.2. Strongly Attractive (SA) Disjoining Pressure. In the strongly attractive (SA) case, the mercury interface is positively charged, so the electrical double layer interaction with the negative mica surface gives a disjoining pressure that is monotonically attractive (see Figure 1). A comparison between experimentally observed profiles of the mercury/electrolyte interface $h(r, t)$ with theoretical predictions using the data in Table 1 is given in Figure 6a.

In this case, instead of forming a stable equilibrium film, the mercury surface collapses onto the mica surface because of the strongly attractive disjoining pressure. This collapse is very rapid, as the observed jump of the mercury/electrolyte interface into contact with the mica surface occurred within one video frame of the last recorded profile at $t = 0.64$ s (see Figure 6). The predicted theoretical profile at $t = 0.66$ s (corresponding to the next video frame) is also shown in Figure 6 to illustrate that the barrier rim has jumped 50 nm or more toward the mica surface.

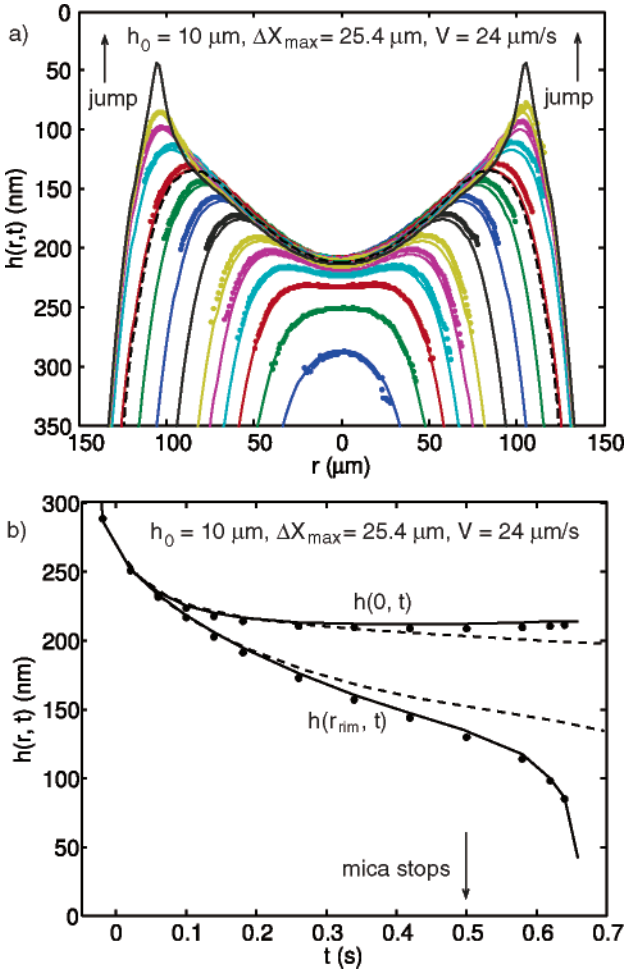

Figure 6. Comparison between theory (lines) and experiment (points) for strongly attractive (SA) disjoining pressure. (a) Drop profiles $h(r, t)$ from bottom to top: $t = -0.02$, 0.02, 0.06, 0.1, 0.14, 0.18, 0.26, 0.34, 0.42, 0.497 (dashed − mica stops), 0.5, 0.58, 0.62, and 0.64 s. The theoretical profile at the next video frame at $t = 0.66$ s is also shown. (b) Film thickness at the center $h(0, t)$ and at the barrier rim $h(r_{rim}, t)$. The experimental results for the strongly repulsive (SR) case (dashed lines) from Figure 2b are included for comparison.

In reality, it is expected that the rupturing process of the trapped dimple is likely to occur in an asymmetric manner that will not be reproduced in an axially symmetric model considered here. Nonetheless, the agreement between theory and experiment before the jump-in is gratifying, as is the fact that the theory predicts accurately the time at which the film collapse occurs.

From the results in Figures 2a, 6a, and 6b, we can see that, at large separations ($h \geq 200$ nm), the mercury interfaces are almost identical for the SR and SA cases. This is in accord with the disjoining pressure results in Figure 1 where, for the SA case, the electrical double-layer attraction only becomes significant below about 200 nm and demonstrates that deformations in this large separation regime are only dependent on the long-range hydrodynamic interactions.

In Figure 6b, we compare experimental time variations of the film thickness at the center of the dimple, $h(0, t)$, and the film thickness at the barrier rim, $h(r_{rim}, t)$, with theoretical predictions. Again, the agreement is very good.

The pressure profiles calculated from our theory that correspond to the strongly attractive case are shown in Figure 7. We observed that, up until just prior to the collapse of the dimple, the total pressure remains essentially constant even though individually

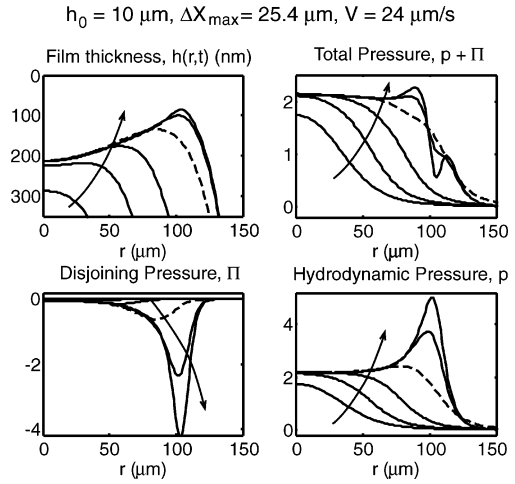

Figure 7. Variations of the hydrodynamic pressure p, disjoining pressure Π, and total pressure ($p + \Pi$) for the strongly attractive (SA) case with initial separation $h_0 = 10\ \mu$m, mica travel $\Delta X_{max} = 25.4\ \mu$m, and mica velocity $V = 24\ \mu$m/s (same parameters as results in Figure 6): $t = -0.02$, 0.1, 0.26, 0.497 (dashed − mica stops), 0.62, and 0.64 s. The arrow indicates increasing time.

the hydrodynamic and disjoining components begin to show large spatial variations, which mutually cancel.[27]

4.3. Weakly Attractive (WA) Disjoining Pressure. The comparison between experiment and theory for the weakly attractive case is given in Figure 8. In this case, the disjoining pressure curve is repulsive at large separations, possesses a small maximum at around 50 nm that is less than the Laplace pressure of the drop (see Figure 1), and is attractive at separations below about 40 nm. While the mica surface was driven toward the mercury drop at constant velocity for about 1 s and was then stopped, the drainage process continued further for about 18 s before the film collapsed—a time that is predicted accurately by the theory. The agreement between theory and experiment at intermediate times during the film drainage process is not as close as for the strongly repulsive or strongly attractive case, but the calculations still reproduce all the features reasonably well, including a "bounce" in which $h(0, t)$ increases for a short time after the drive stops. No bounce occurs in the SA or SR cases, but it is observed in both the data and the computation for the WA case.

Our attempts to fit the weakly repulsive (WR) data from ref 4 were unsuccessful for any reasonable combination of parameters in the model. This is puzzling, given the success in fitting the other three cases, and we are led to believe that the experimental WR data set may be flawed. A possible reason is that insufficient time was allowed for equilibration of the mercury drop after changing applied potential between the SR and WR measurements.

5. Predictions of the Model

The comparisons given in the previous section provide compelling evidence that our theoretical model is capable of providing an accurate description of the thin film drainage process under the action of repulsive and attractive surface forces. We can now examine the model for information that was not accessed or is not accessible experimentally.

The experimental profiles show sub-micrometer dimpling in a millimeter mercury drop relative to the mica surface. Using the model, we can quantify the relative extent of the deformations by viewing the deforming drop on different length scales. The key features are illustrated in Figure 9 for the strongly repulsive (SR) interaction. In the rear panel, the drop is shown on a

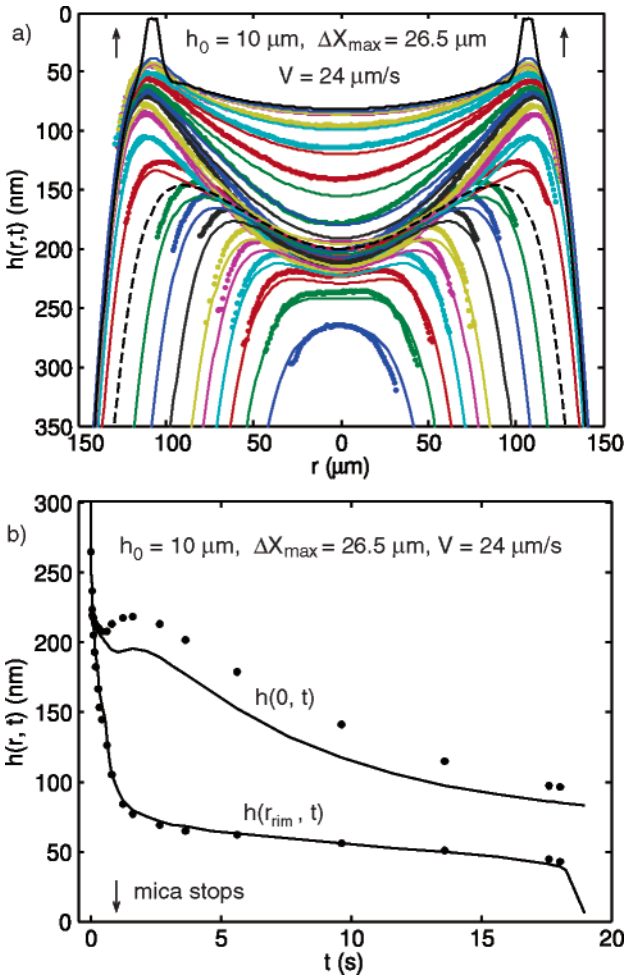

Figure 8. Comparison between theory (lines) and experiment (points) for the weakly attractive (WA) disjoining pressure. (a) Drop profiles from bottom to top: $t = -0.02$, 0.02, 0.06, 0.1, 0.14, 0.18, 0.26, 0.34, 0.42, 0.51 (dashed − mica stops), 0.62, 0.82, 1.22, 1.62, 2.62, 3.62, 5.62, 9.62, 13.62, 17.62, 18.02, and 19 s. (b) Film thickness at the center $h(0, t)$ and at the barrier rim $h(r_{rim}, t)$.

millimeter scale, which makes it clear that the deformation and interaction zone are confined to a region ~300 μm in radius, which is small compared to the size of the drop. Moreover, on this scale, it appears that the mercury drop and the mica are in contact. In the middle panel of Figure 9, we show the drop profiles drawn on the 100-μm scale. Once again, on this scale, mica and the mercury drop seem to be in contact, and dimpling of the mercury/electrolyte interface is not yet visible. The nanometer-scale dimpling and film thickness, as measured in the experiment, are shown in the front panel of Figure 9.

The amount of deformation in the mercury interface, that is, the difference in height between the actual interface and its undeformed spherical shape, as time evolves is shown in Figure 10 for the strongly repulsive case. As can be seen, when the first experimental profile is measured, the mercury drop has already deformed about 4 μm at $r = 0$, since the mica has already travelled for about 14 μm from an initial separation of 10 μm. Note that, after the mica has stopped, further deformations of the mercury interface are very small on the micrometer scale shown in Figure 10. However, on the nanometer scale, the dimple still continues to evolve (see Figure 2).

The relative velocity between the mercury/electrolyte interface and the mica is plotted in Figure 11. Initially, the magnitude of the relative velocity of all parts of the mercury/electrolyte is 24 μm/s, which is the velocity of the mica. As the film thins, the

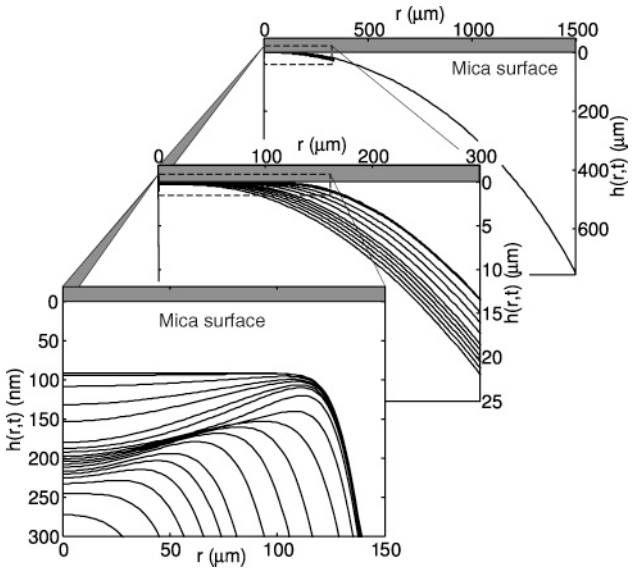

Figure 9. Views of the deforming mercury/electrolyte interface on different length scales to illustrate nanometer deformations on a millimeter drop for the strongly repulsive case: initial separation $h_0 = 10\ \mu$m, mica travel $\Delta X_{max} = 27.1\ \mu$m, and mica velocity $V = 24\ \mu$m/s for $t = -0.02$ to 13.62 s.

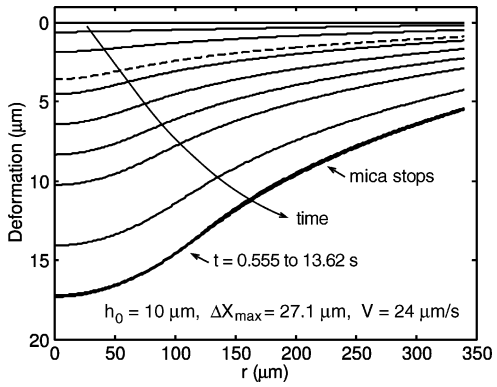

Figure 10. Deformation of the mercury interface as the mica approaches for the strongly repulsive (SR) case. From bottom to top: $t = -0.575$, -0.2, -0.1, -0.02 (dashed curve − first experimental profile), 0.02, 0.1, 0.18, 0.26, 0.42, 0.555 (mica stops), 0.62, 0.82, 1.22, 1.62, 2.62, 3.62, 5.62, 9.62, and 13.62 s.

mercury interface starts to deform, and the relative velocity in the center of the film decreases in magnitude. By the time the first profile is measured ($t = -0.02$ s), the approach velocity is almost zero in the center, while the velocity at r_{max} is around two-thirds of the mica velocity. When the mica stops at $t = 0.555$ s, the velocity at r_{max} is about half the mica velocity. After the mica stops, the magnitude of the relative velocity decreases to values $\ll 1\ \mu$m/s.

5.1. Hydrodynamic Effects. To illustrate the effects of hydrodynamic interactions in film thinning in our system, we present some theoretical results in the absence of disjoining pressure, $\Pi = 0$, but otherwise under the same experimental conditions as those in Figure 2.

In Figure 12a, we show the evolution of the film thickness under the experimental protocol in which the mica surface is driven at constant velocity toward the mercury drop for a predetermined time and then stopped. In this case, the aqueous film and dimple that is formed will drain very slowly. In the absence of a repulsive disjoining pressure to maintain a minimum value for the barrier rim thickness $h(r_{rim}, t)$ to facilitate drainage

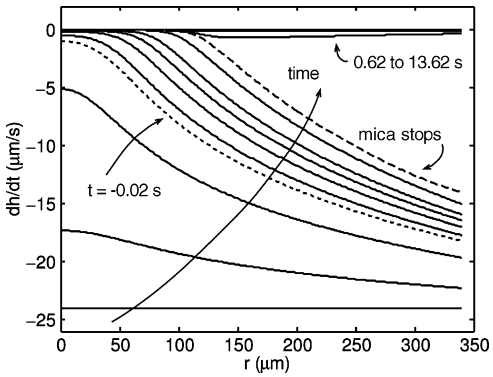

Figure 11. Relative velocity of approach between the mercury/electrolyte interface and the mica for the strongly repulsive (SR) case: initial separation $h_0 = 10\ \mu$m, mica travel $\Delta X_{max} = 27.1\ \mu$m, and mica velocity $V = 24\ \mu$m/s for $t = -0.575$, -0.2, -0.1, -0.02 (dashed curve − first experimental profile), 0.02, 0.1, 0.18, 0.26, 0.42, 0.555 (mica stops), 0.62, 0.82, 1.22, 1.62, 2.62, 3.62, 5.62, 9.62, and 13.62 s.

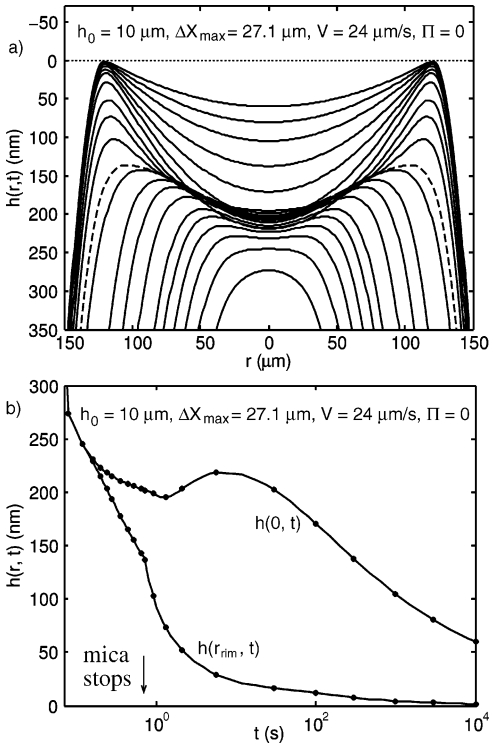

Figure 12. Predictions of the evolution of the mercury/electrolyte in the absence of a disjoining pressure ($\Pi = 0$) where the initial separation h_0, the velocity V, and the total push ΔX_{max} were chosen to be the same as in the strongly repulsive (SR) case (see Figure 2). (a) Drop profiles from bottom to top: $t = -0.02$, 0.02, 0.06, 0.10, 0.14, 0.18, 0.26, 0.34, 0.42, 0.555 (dashed curve − mica stops), 0.62, 0.82, 1.22, 2.62, 13.62, 30, 100, 300, 1000, 3000, and 10000 s. (b) Film thickness at the center $h(0, t)$ and barrier rim $h(r_{rim}, t)$. Dots indicate the time steps plotted in part a. Note the logarithmic scale of t.

of fluid trapped in the dimple or an attractive disjoining pressure to cause the collapse of the intervening film, the barrier rim thickness thins very slowly and takes $\sim 10^4$ s to reach subnanometer thickness, beyond which a continuum hydrodynamic model for the intervening film ceases to be valid. An interesting observation, made clear in Figure 12b, is that the film thickness at the center, $h(0, t)$, initially decreases with time as expected but then increases to a maximum at $t \sim 10$ s and then finally decreases again. Such a maximum or "bounce" in the behavior

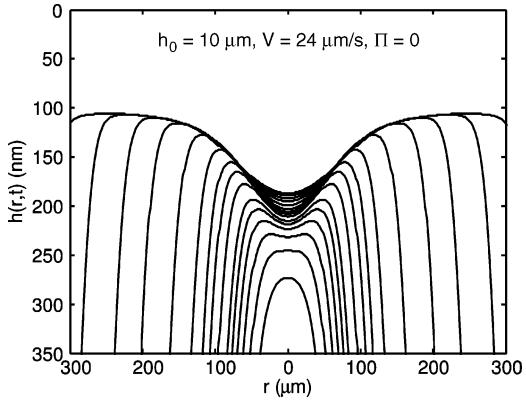

Figure 13. Predictions of the evolution of the mercury/electrolyte in the absence of a disjoining pressure ($\Pi = 0$) where the initial separation h_0 and the velocity V were chosen to be the same as in the strongly repulsive (SR) case (see Figure 2), but the mica was driven continuously. Drop profiles from bottom to top: $t = -0.02$, 0.02, 0.06, 0.10, 0.14, 0.18, 0.26, 0.34, 0.42, 0.62, 0.82, 1.22, 1.62, and 2.62 s.

of $h(0, t)$ is detectable in cases where the disjoining pressure in the system is small, such as the weakly attractive case shown in Figure 8.

A cusp is observed in the plot of $h(r_{rim}, t)$ in Figure 12b at the point where the mica drive stops. At this time, the approach conditions change from constant speed to quasi-constant force. The force between the drop and the mica surface is associated with the macroscopic deformation of the drop, which changes very little after the mica stops moving (Figure 10). The cusp indicates an increase in the approach rate of the barrier rim when the drive changes from quasi-constant speed to constant force, consistent with the results in Klaseboer et al.[14] and Yiantsios and Davis.[22] This "closing down" of the barrier rim forces some of the aqueous phase back into the dimple, which has the effect of forcing an increase in h_0 at a slightly later time (the bounce), before the drainage continues again in the usual direction of film thinning.

The stabilizing influence of hydrodynamic interactions is illustrated in Figure 13 in which the mica surface is driven continually, without stopping, toward the mercury interface again in the absence of disjoining pressure ($\Pi = 0$). Here, we see that at $t = 2.62$ s (the last profile plotted in Figure 13) where the mica has traveled 76.7 μm, the film thickness remains over 100 nm but the radial position of the barrier rim continues to increase. Thus, the repulsion arising from hydrodynamic interactions alone drastically reduced the film thinning rate.

5.2. Shear Rates and Flow in the Film. In Figure 14, we present results for the shear rate $(dv_r/dz)(r, t)$ evaluated at the mica/electrolyte interface for the strongly repulsive (SR) case. These give insight into details of fluid flow within the draining film. From Figure 14a,b for the shear rate as a function of radial position on the mercury surface, we observe that the profile for the shear rate grows in magnitude as the mica surface approaches the mercury drop. The profile reaches a maximum just before $t = 0$, then it starts to decrease because the mean radial velocity in the intervening film begins to fall. During the drainage phase (Figure 14b), the shear rate profiles continue to decrease as the drainage process slows down. In Figure 14c, we show the variation of the maximum value of the shear rate with time. The small maximum in the shear rate at the time when the mica is stopped is a consequence of the discontinuity in acceleration as the mica stops. We see that, during the drainage of the dimple across the narrow gap at the barrier rim, the shear rate is less than 10^3 s^{-1}. In Figure 14d, we present the time variation of the position of

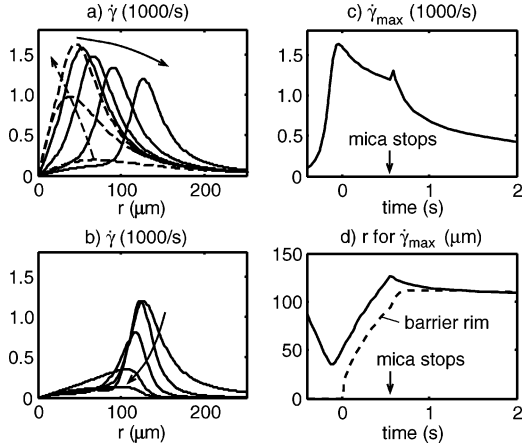

Figure 14. Behavior of the shear rate ($\dot{\gamma}$) at the mercury/electrolyte interface for the strongly repulsive (SR) case corresponding to results presented in Figure 2. (a) During mica approach: $t = -0.3$, -0.15, -0.02, 0.02, 0.1, 0.26, and 0.555 s (mica stops). The 3 first profiles (dashed lines) correspond to $t < 0$. (b) During drainage after the mica has stopped: $t = 0.555$, 0.62, 0.82, 1.62, and 5.62 s. (c) Maximum value of the shear rate ($\dot{\gamma}_{max}$) as a function of time. (d) Radial position of the maximum in the shear rate (solid line) and barrier rim (dashed line). The arrows indicate increasing time.

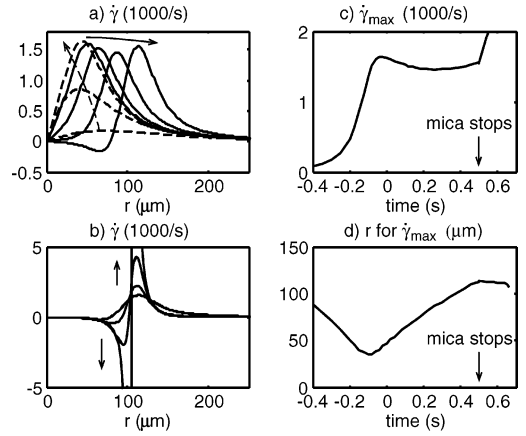

Figure 15. Behavior of the shear rate ($\dot{\gamma}$) for the strongly attractive (SA) case from Figure 6. (a) During mica approach: $t = -0.3$, -0.15, -0.02, 0.02, 0.1, 0.26, and 0.497 s (mica stops). (b) 0.497, 0.58, 0.64, and 0.66 s. (c) Maximum value of the shear rate ($\dot{\gamma}_{max}$) as a function of time. (d) Radial position of the maximum in the shear rate. The arrows indicate increasing time.

the maximum in the shear stress at the mercury surface. We see that after the formation of the dimple the maximum is located close to but slightly outside the barrier rim.

In Figure 15, we present shear rate results for the strongly attractive (SA) case. The results in Figure 15a show similar features as in the SR case during approach. This is expected, since double-layer interactions are unimportant at large separations during these early times. However, after the mica stops (Figure 15b), the magnitude of the shear rate begins to increase significantly. This is caused by the attractive disjoining pressure that, at this stage, is acting to pull the mercury surface toward the mica. The accelerated thinning at the barrier rim due to attractive disjoining pressures increases the shear rate and outflow velocity in the radial position just beyond the barrier rim. However, at radial positions inside the barrier rim, the shear rate has become negative, so the flow of the intervening fluid is directed toward the center of the dimple at $r = 0$. This radially inward flow then causes the film thickness at the center of the dimple to decrease more slowly than the in SR case (see Figure 6b). Analysis of shear rates in the calculations without disjoining pressure

presented in section 5.1 also shows a region of negative shear rate close to but inside the barrier rim at times shortly after the drive stop time. Again, this indicates a flow of liquid toward $r = 0$ within the film, as required for the observed bounce in $h(0, t)$ to occur (Figure 12).

6. Discussion

We have made a detailed comparison between experimental observations and theoretical predictions for the thinning of an aqueous film between an approaching mica plate and a deformable mercury drop under both repulsive and attractive electrical double-layer forces between the interfaces. Like other theoretical models already in the literature, ours is based on the Young−Laplace equation, Reynolds lubrication theory, and the inclusion of a disjoining pressure to account for surface forces. However, an important feature of the present theory is that it includes consideration of the far-field deformation of the fluid drop. As seen in Figure 10, the deformation is significant in regions of the drop well beyond the barrier rim, where hydrodynamic pressures are very small and surface forces are negligible. Proper consideration of far-field deformation allows modeling of the experimental situation for any prescribed drive function of a solid approaching a drop that is held at a fixed capillary. More generally, the present approach can be readily extended to other modes of interaction between deformable drops which may be driven by externally imposed flow fields and/or are under the effects of thermal motion.

The theoretical model provides good fits to the experimental data, which encourages one to believe that the physics on which it is based is sound and the approximations and assumptions made are reasonable. It is of particular interest that no-slip boundary conditions were required to provide agreement with experimental data, not only at the mica/electrolyte interface but also at the mercury/electrolyte interface. It was noted at the outset that these assumptions were made in the interest of starting with a simple model. The fact that the model has been shown to fit the data gives a posteriori justification to the assumptions.

We assess the possible influence of slip at either interface by assuming that the mercury/electrolyte interface has slip length b_h and the mica/electrolyte interface has slip length b_0 and use the Navier slip length model defined by the following boundary conditions:

$$u_r = b_0 \frac{\partial u_r}{\partial z} \quad \text{at } z = 0 \tag{16}$$

$$u_r = -b_h \frac{\partial u_r}{\partial z} \quad \text{at } z = h \tag{17}$$

This model still assumes that there is no flow inside the mercury drop. Equations 16 and 17 add a linear component to the flow profile, and the time evolution of the thickness of liquid film between the drop and the mica is now described by[28]

$$\frac{\partial h}{\partial t} = \frac{1}{12\mu r}\frac{\partial}{\partial r}\left(rh^3\frac{\partial p}{\partial r}\right) + \frac{1}{4\mu r}\frac{\partial}{\partial r}\left\{r\frac{\partial p}{\partial r}\left[\frac{(b_h + b_0)h^3 + 4b_0b_hh^2}{h + b_h + b_0}\right]\right\} \tag{18}$$

In Figure 16, we compare the time dependence of the central film thickness $h(0, t)$ for various values of slip length b_h at the mercury interface for the SR case, while the no-slip ($b_0 = 0$) boundary condition is applied at the mica surface (see also Figure 2). Here, we see that, even with the no-slip condition ($b_h = 0$), the predicted form of $h(0, t)$ already thins a little faster than experimental values. The allowance of any degree of slip only increases the divergence between theory and experiment. We stress that our results in sections 4 and 5 are obtained with eq 2, which corresponds to the no-slip boundary condition at the interfaces.

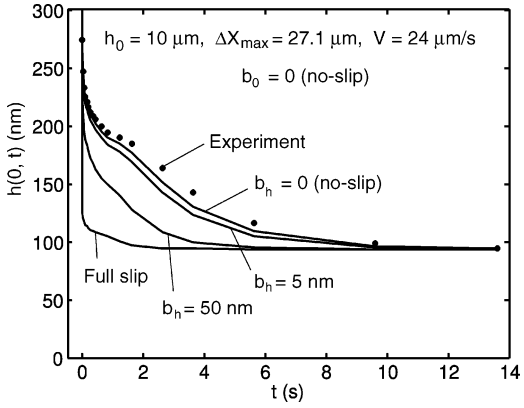

Figure 16. Film thickness at the center $h(0, t)$, where dots represent the experimental values and lines are solutions based on eq 20 for $b_h = 0$ (no-slip), $b_h = 5$ nm, $b_h = 50$ nm, and $b_h = \infty$ (full slip) at the mercury/electrolyte interface and $b_0 = 0$ at the mica/mercury interface. The initial separation h_0, mica travel ΔX_{max}, and mica velocity V are indicated in the figure.

There are a number of reports in the recent literature[29] that purport to show that partial slip occurs at many solid/liquid interfaces and follows the Navier slip boundary condition. Slip lengths ranging from ~10 nm up to a few micrometers have been reported, although other reports find that the no-slip boundary condition applies within 1−2 nm of the solid/fluid interface. Allowing slip at the mica/electrolyte interface ($b_0 > 0$) in our model would make agreement with experiment worse, similar to what is shown in Figure 16, since b_0 and b_h are interchangeable in eq 18. Our results therefore lead to the conclusion that a no-slip boundary condition applies within 1 or 2 nm of the solid/liquid interface, at least for the conditions of our experiment—aqueous electrolyte against a smooth hydrophilic solid, with shear rates up to $\sim 10^3$ s^{-1}.

At the mercury/electrolyte interface, the classical expectation is that a partial-slip condition should hold, because these two liquids have comparable viscosities. Our model neglects fluid circulation within the mercury drop and assumes that the radial component of the velocity of water at the mercury/electrolyte interface is zero. With these assumptions, we are able to obtain a good fit to experimental data. By adjusting other physical parameters to the extremes allowed by experimental uncertainty, it is possible to accommodate a slip length of no larger than 2 nm at each interface while still being able to maintain a reasonable fit between theory and experiment. The use of a full-slip boundary condition at either interface would have yielded film drainage times 10 times shorter than those observed experimentally (see Figure 16). In our view, there is no compelling need to invoke the slip length as an additional parameter to fit experiments, and our results support the conclusion of zero or negligible slip at the interfaces.

We further remark that the minor deviations between theory and experiment in the above figures generally show that the theory predicts faster thinning of the film near $r = 0$ and perhaps

(28) Vinogradova, O. I. *Langmuir* **1996**, *12*, 5963.

(29) Neto, C.; Evans, D. R.; Bonaccurso, E.; Butt, H.-J.; Craig, V. S. J. *Rep. Prog. Phys.* **2005**, *68*, 2589.

slightly slower near the barrier rim (see, for example, Figure 2a). While allowing a small degree of slip can improve the agreement near the barrier rim, it would then also necessitate increasing the velocity to the limit of experimental uncertainty to generate the same extent of dimpling, and of course, the agreement between theory and experiment near $r = 0$ will deteriorate. Similarly, if the theory were extended to include consideration of fluid circulation within the mercury drop, the film drainage would be faster, and agreement with experiment would be made worse rather than better.

The fact that our data are consistent with a no-slip boundary condition at the mercury/electrolyte interface requires further discussion. A no-slip boundary condition is known to occur at fluid/fluid interfaces if sufficient surfactant (less than a monolayer) is adsorbed to immobilize the interface. In the experiments reported in ref 4, strenuous efforts were made to minimize contamination in both the mercury and aqueous phases and to work with a freshly prepared mercury/electrolyte interface no more than ~10 min old, but it is never possible to guarantee that the level of surface-active material was zero. Hence, it is impossible to state unequivocally that the absence of slip that seems to fit our experimental data was not caused by immobilization of the interface by trace contaminants. However, other experimental data—measurements of surface forces[8] and of mercury/electrolyte interfacial tension—gave no indication that the interface was contaminated.

There is also the possibility that, in the presence of adsorbed surface-active species, compression or redistribution of such species along the interface can occur as a result of hydrodynamic flow in the adjacent fluids, giving rise to the Marangoni effect.[30,31] Such coupling between fluid flow and adsorbate distribution in the interface acts to retard the flow, which is the direction required to improve agreement between theory and experiment within the dimple region. However, it can only be effective if the amount of surfactant at the interface is less than the amount required to immobilize the interface—no Marangoni effect can occur if there are no-slip boundary conditions. Hence, inclusion of Marangoni coupling would require use of a partial-slip boundary condition as a starting point, which as we have discussed above is not consistent with our data.

Apart from the question of hydrodynamic boundary conditions discussed above, there is another factor that could possibly account for the minor discrepancy between theory and experiment near $r = 0$. The discrepancy would be removed if a small additional pressure (~20 Pa, or ~5% of the Laplace pressure in the drop) were acting in a region of radius 50 μm around $r = 0$, and a possible source is osmotic pressure due to a locally high concentration of solute. An additional concentration of 8 μM in this central region is all that would be required to produce 20 Pa of pressure. In this regard, there is one experimental detail that has not been considered thus far in the discussion. While mercury is generally regarded as a perfectly polarizable electrode, we in fact observe a small leakage current of about 0.3 μA throughout the experiment. The current may be associated with an electrode process that produces new molecular or ionic species, such as reduction of oxygen that remains dissolved at trace levels in the aqueous phase despite our best efforts to remove it. The portion of leakage current in the interaction zone (of lateral radius ~100 μm and thickness ~100 nm) would be sufficient to generate a significant concentration of new solute (as much as 1 mM each second) in the small volume of the aqueous film. If the new solute is slow to diffuse out of this constricted region, a local increase in osmotic pressure could easily be accounted for. While a detailed consideration of this effect will require additional experimentation and consideration of solute transport parallel to the trapped electrolyte film, we can see that the difference between theory and experiment in the interfacial profile around $r = 0$ could be caused by small local variations in solute concentration.

Interestingly, both experiment and theory show that the mercury continues to approach the mica after the latter has stopped moving. In particular, not only does $h(0, t)$ continue to decrease as the dimple relaxes, but $h(r_{rim}, t)$ also decreases. This cannot be an effect of inertia of any of the media involved, since inertia is not included in the model. Instead, it is associated with the experimental design, which has a transition from constant velocity while the mica is being driven to quasi-constant force after the drive stops. The drop shape continues to evolve from its instantaneous shape at t_{stop} to its equilibrium shape under the influence of disjoining pressure and hydrodynamic effects. This includes a change in the far-field deformation, which drives a continuing evolution of the barrier rim. As seen from Figure 12, the film thickness $h(r_{rim}, t)$ at the barrier rim actually decreases more rapidly after the drive stops. In the absence of disjoining pressure or in the presence of an attractive disjoining pressure, this can push some of the aqueous phase back toward the center of the dimple and causes the "bounce" in $h(0, t)$ that is seen in Figures 8 and 12.

A particular feature of our experimental modeling is the success in predicting the time at which the aqueous film collapses when the disjoining pressure is weak or attractive. Experimentally, the collapse is observed to occur very quickly, but we are unable to say whether it involves processes that are not axisymmetric and/or multiple local collapses and/or engulfment of the aqueous film phase inside the mercury drop. However, the model does predict the moment of collapse accurately, which strongly suggests that the physical phenomena causing the collapse are included in the model. If we remember that the model is strictly axisymmetric, this means that the collapse is predicted without any reference to capillary waves or local instabilities of the film. Instead, the implication is that the collapse is determined by a mechanical instability in which the gradient of disjoining pressure overcomes the ability of the drop to resist, through its interfacial tension, a sudden elongation.

In summary, the agreement we have found between our theoretical model and accurate experimental data instills confidence in using the theoretical model to infer details of the film drainage process. The model can now be applied to understanding related phenomena such as the stability of drop−drop interactions, drop deformation under different approach conditions, drop coalescence, and more generally the interaction between soft bodies. These will be the subject of future investigations.

Acknowledgment. This work was supported in part by a Discovery Project Grant of the Australian Research Council (ARC) and by two ARC Special Research Centres − the Particulate Fluids Processing Centre at the University of Melbourne, and the SRC for Particle and Material Interfaces at the Ian Wark Research Institute. R.M. is supported by a University of Melbourne International Research Scholarship.

LA0620760

(30) Traykov, T. T.; Ivanov, I. B. *Int. J. Multiphase Flow* **1977**, *3*, 471.
(31) Chesters, A. K.; Bazhlekov, I. B. *J. Colloid Interface Sci.* **2000**, *230*, 229.